

THEORETICAL DESCRIPTION OF GRB 160625B WITH WIND-TO-ISM TRANSITION AND IMPLICATIONS FOR A MAGNETIZED OUTFLOW

N. FRAIJA^{1†}, P. VERES², B. B. ZHANG³, R. BARNIOL DURAN⁴, R. L. BECERRA¹, B. ZHANG⁵, W. H. LEE¹, A. M. WATSON¹, C. ORDAZ-SALAZAR¹ AND A. GALVAN-GAMEZ¹

¹ Instituto de Astronomía, Universidad Nacional Autónoma de México, Circuito Exterior, C.U., A. Postal 70-264, 04510 México D.F., México.

² Center for Space Plasma and Aeronomic Research (CSPAR), University of Alabama in Huntsville, Huntsville, AL 35899, USA

³ Instituto de Astrofísica de Andalucía (IAA-CSIC), P.O. Box 03004, E-18080 Granada, Spain

⁴ Department of Physics and Astronomy, Purdue University, 525 Northwestern Avenue, West Lafayette, IN 47907, USA

⁵ Department of Physics and Astronomy, University of Nevada Las Vegas, Las Vegas, NV 89154, USA

Draft version September 12, 2017

ABSTRACT

GRB 160625B, one of the brightest bursts in recent years, was simultaneously observed by Fermi and Swift satellites, and ground-based optical telescopes in three different events separated by long periods of time. In this paper the non-thermal multiwavelength observations of GRB 160625B are described and a transition phase from wind-type-like medium to interstellar medium between the early (event II) and the late (event III) afterglow is found. The multiwavelength observations of the early afterglow are consistent with the afterglow evolution starting at ~ 150 s in a stellar wind medium whereas the observations of the late afterglow are consistent with the afterglow evolution in interstellar medium (ISM). The wind-to-ISM transition is calculated to be at $\sim 8 \times 10^3$ s when the jet has decelerated, at a distance of ~ 1 pc from the progenitor. Using the standard external shock model, the synchrotron and synchrotron self-Compton emission from reverse shock is required to model the GeV γ -ray and optical observations in the early afterglow, and synchrotron radiation from the adiabatic forward shock to describe the X-ray and optical observations in the late afterglow. The derived values of the magnetization parameter, the slope of the fast decay of the optical flash and the inferred magnetic fields suggest that Poynting flux-dominated jet models with arbitrary magnetization could account for the spectral properties exhibited by GRB 160625B.

Subject headings: gamma-rays bursts: individual (GRB 160625B) — radiation mechanisms: nonthermal

1. INTRODUCTION

Gamma-ray bursts (GRBs) are the most luminous explosions in the universe. Observations have firmly established that GRB prompt phases and their afterglows arise from highly relativistic and collimated outflows (Panaitescu & Kumar 2002; Taylor et al. 2004; Kumar & Zhang 2015). Long GRBs (IGRBs) have been associated to the core collapse of massive stars (Woosley & Bloom 2006; Hjorth & Bloom 2012; Hjorth et al. 2003). According to the collapsar model, IGRBs are generated in shocks that take place after the ultra relativistic jet has broken out from the stellar envelope. The jet dynamics is mainly dominated by the jet head, which is controlled by the difference in pressures between the reverse and forward shocks. If the luminosity is low enough and/or the density of stellar envelope is high enough, the collimated jet will then be surrounded by a cocoon (Mizuta & Ioka 2013; Bromberg et al. 2011; Ramirez-Ruiz et al. 2002). When the relativistic jet is going through the progenitor star, its rate of advance is slowed down and most of the energy output during this phase is deposited into the cocoon. It starts spreading up to the optical depth becomes equal to unity and then, an X-thermal component could be expected.

The description of bright optical flashes by reverse shocks (Gao et al. 2015; Fraija et al. 2016a; Vestrand et al. 2014; Huang et al. 2016; Zhang et al. 2003) and the high degree of optical polarization detected in some bursts (Gorbovskoy et al. 2016; Pruzhinskaya et al. 2014; Kopač et al. 2015; Steele et al. 2009; Mundell et al. 2007; Troja et al. 2017; Mundell et al. 2013) have supplied strong evidence that sources could

be endowed with magnetic fields (Usov 1992; Coburn & Boggs 2003; Wheeler et al. 2000). Using standard assumptions such as the reverse-shocked shell carries a substantial energy, optical flashes are described by synchrotron emission from reverse shock which is shown as a single peak (Chevalier & Li 2000; Zhang & Kobayashi 2005; Zhang et al. 2003; Kobayashi & Zhang 2003a; Kobayashi 2000) and then high-energy photons could be generated by inverse Compton scattering process (Wang et al. 2001a,b; Kobayashi et al. 2007; Fraija 2015; Fraija et al. 2016b).

Ackermann et al. (2013) reported the first Fermi-LAT catalog which summarized the temporal and spectral properties of the 28 GRB LAT-detected above 100 MeV and 7 GRBs above ~ 20 MeV. These bursts were recorded since the beginning of nominal science operations in 2008 until 2011. Analysis of the high-energy emission showed that the more luminous bursts present a bright and short-lasting peak at the end of the prompt emission and a temporally extended component lasting hundreds of seconds.

GRB160625B was detected on 2016 June 25 by both instruments on board Fermi satellite; Gamma-Ray Burst Monitor (GBM; Burns 2016) and Large Area Telescope (LAT; Dirirsa et al. 2016), XRT and UVOT instruments on board Swift satellite (Melandri et al. 2016) and several optical telescopes (CASANDRA all-sky cameras on the BOOTES-1 and -2 astronomical stations, Mini-Mega TORTORA, the Pi of the Sky observatory, TSHAO, AbAO, RATIR, Mondy, CrAO, Maidanak and SAO RAS. See, Zhang et al. 2016; Troja et al. 2016). This burst was originally divided in three different temporal events. Zhang et al. (2016) stated that the spectral properties of the first two sub-bursts transition (from thermal to non-

thermal radiation in a single burst) indicated the variation of the jet composition from a fireball to a Poynting-flux dominated jet. Lü et al. (2017) proposed that the event I could be explained by the cocoon emission surrounding the jet, the early afterglow by the superposition of the photosphere and internal shock emissions and finally, the late afterglow by the emission generated in both internal and external shocks.

In this paper, we use the early-afterglow external shock model in stellar wind medium and interstellar medium (ISM) to describe the multiwavelength observations during events II (henceforth called early afterglow) and III (henceforth called late afterglow) of GRB 160625B. The paper is arranged as follows. In Section 2 we show the dynamics of external shocks that evolves adiabatically in a stellar wind-type-like medium and ISM. In Section 3 we present the multiwavelength observations, data reduction and data analysis. In Section 4, the discussion and results on the analysis done to the multiwavelength data are presented. Finally, in Section 5 we give a brief summary.

2. DYNAMICS OF THE EXTERNAL SHOCKS

The external shocks take place when the relativistic ejecta collide with the circumburst medium and start to be slowed down. Generally, an ongoing shock that propagates into the surrounding medium so-called forward shock and a reverse shock that propagates into the flow are formed. The afterglow phase begins when the ejecta has swept enough material so that most of the energy of the ejecta has been transferred to the circumburst medium. We present the afterglow evolution in a stellar wind medium and ISM, and the wind-to-ISM transition.

2.1. Afterglow evolution in the stellar wind-type-like medium

The dynamics of a relativistic shell interacting with the surrounding medium with an inhomogeneous density (stellar wind-like medium) has been widely discussed (e.g. see, Chevalier & Li 2000). For the adiabatic blast wave, the typical timescales (deceleration, cooling and acceleration), the deceleration radius, the Lorentz factors, the synchrotron spectral breaks, the maximum flux and synchrotron light curves are given in Chevalier & Li (1999, 2000); Panaitescu & Kumar (2000). Using the previous quantities, the synchrotron flux in the fast-cooling regime is proportional to $\propto t^{-\frac{3p-2}{4}} E^{-\frac{p}{2}}$ for $E_{m,f}^{\text{syn}} < E^{\text{syn}} < E_{\text{max},f}^{\text{syn}}$ and $\propto t^{-\frac{1}{4}} E^{-\frac{1}{2}}$ for $E_{c,f}^{\text{syn}} < E^{\text{syn}} < E_{m,f}^{\text{syn}}$, where $E_{c,f}^{\text{syn}}$, $E_{m,f}^{\text{syn}}$ and $E_{\text{max},f}^{\text{syn}}$ are the synchrotron spectral breaks for the cooling, characteristic and maximum photon energy, respectively (i.e. Gao et al. 2013a). In the slow-cooling regime, the synchrotron flux is proportional to $\propto t^{-\frac{3p-1}{4}} E^{-\frac{p-1}{2}}$ for $E_{m,f}^{\text{syn}} < E^{\text{syn}} < E_{c,f}^{\text{syn}}$ and $\propto t^{-\frac{3p-2}{4}} E^{-\frac{p}{2}}$ for $E_{c,f}^{\text{syn}} < E^{\text{syn}} < E_{\text{max},f}^{\text{syn}}$. Relativistic electrons accelerated in the forward shocks could scatter synchrotron photons up to energies larger than 100 MeV. The synchrotron self-Compton (SSC) light curves with their spectral breaks are described in detail in Fraija et al. (2016a). For reverse shocks, the observables of synchrotron radiation such as synchrotron spectral breaks, fluxes and synchrotron light curves that describe the optical flashes are derived in Chevalier & Li (2000). For instance, in the thick-shell regime and in the optical energy range, synchrotron flux increases proportionally to $t^{1/2}$, reaching a maximum at the peak time of $t_d \sim \left(\frac{\Gamma_d}{\Gamma_c}\right)^{-4} T_{90}$ and after the peak, it decays fast $\propto t^{-(\beta+2)}$ dominated by the angular time delay effect

in higher latitude emissions (Kumar & Panaitescu 2000a). Here, Γ_c is the critical Lorentz factor, $\Gamma_d \sim \min(\Gamma, 2\Gamma_c)$ is the bulk Lorentz factor at the shock crossing time and T_{90} is the duration of the burst. The spectral index β corresponds to the low- and high-energy power-law indexes $1/2$ and $p/2$, respectively. The optical flux at the peak is derived and written explicitly in Kobayashi & Zhang (2003a). These authors discussed the optical light curve generated in the reverse shock by the angular time delay effect produced by the high latitude emission. For the cooling energy ($E_{c,r}^{\text{syn}}$) less than that characteristic energy ($E_{m,r}^{\text{syn}} \sim 1$ eV), the angular time delay effect produces a peak followed by a fast decay.

The observables of the SSC emission from a reverse shock such as spectral breaks, fluxes and light curves have been widely explored (e. g. see, Wang et al. 2001a,b; Veres & Mészáros 2012; Fraija et al. 2016a). The SSC light curve around the shock crossing time is derived in Fraija et al. (2016a). For $t < t_d$, SSC flux increases proportionally to $t^{1/2}$ and decreases ($t > t_d$) following a fast decay $\propto t^{-(\beta+2)}$ induced by the angular time delay effect. Again, the spectral index β is $1/2$ and $p/2$ for low and high-energy SSC power laws, respectively. The SSC flux at the peak time $t_d \sim \left(\frac{\Gamma_d}{\Gamma_c}\right)^{-4} T_{90}$ is derived and explicitly calculated in Fraija et al. (2016a).

The duration of the reverse-shock radiation can be calculated through $t_{\text{ang}} \sim (1+z)\theta_j r_{d,SW}$, where $\theta_j \sim \frac{1}{\Gamma_d} \left(\frac{t_j}{t_d}\right)^{1/4}$ could be estimated, in turn, from the jet break time t_j of the synchrotron flux coming from the forward shock (Rhoads 1999; Sari et al. 1999; Kumar & Panaitescu 2000b).

2.2. Afterglow evolution in ISM

The dynamics of the external shocks for the ejecta expanding into a surrounding medium with homogenous density has been widely explored (e.g. see, Sari et al. 1998). Using the synchrotron spectra, the evolution of synchrotron energy breaks and the maximum flux, the synchrotron light curve and spectrum in the fast-cooling regime is proportional to $\propto t^{-\frac{3p-2}{4}} E^{-\frac{p}{2}}$ for $E_{m,f}^{\text{syn}} < E^{\text{syn}} < E_{\text{max},f}^{\text{syn}}$ and $\propto t^{-\frac{1}{4}} E^{-\frac{1}{2}}$ for $E_{c,f}^{\text{syn}} < E^{\text{syn}} < E_{m,f}^{\text{syn}}$ (i.e. van Eerten et al. 2010; Gao et al. 2013a). In the slow-cooling regime, the synchrotron light curve and spectrum is proportional to $\propto t^{-\frac{3p-3}{4}} E^{-\frac{p-1}{2}}$ for $E_{m,f}^{\text{syn}} < E^{\text{syn}} < E_{c,f}^{\text{syn}}$ and $\propto t^{-\frac{3p-2}{4}} E^{-\frac{p}{2}}$ for $E_{c,f}^{\text{syn}} < E^{\text{syn}} < E_{\text{max},f}^{\text{syn}}$, where the proportionality constants of these spectra are explicitly written in e.g., Fraija et al. (2016b).

The achromatic break in the optical and X-ray bands observed in the late afterglow is related to the time when the jet slows down and spreads laterally (Sari et al. 1999). For this case, assuming the synchrotron emission from the same power-law electron distribution and also that the jet break ($\Gamma \sim \theta_j^{-1}$) takes place at time $t_j \propto (1+z)n^{-1/3} E^{1/3} \theta_j^{8/3}$, the synchrotron flux for slow-cooling regime becomes: $\propto t^{-p} E^{-\frac{p}{2}}$ for $E_{c,f}^{\text{syn}} < E^{\text{syn}}$, $\propto t^{-p} E^{-\frac{p-1}{2}}$ for $E_{m,f}^{\text{syn}} < E^{\text{syn}} < E_{c,f}^{\text{syn}}$, and $\propto t^{-1/3} E^{\frac{1}{3}}$ for $E^{\text{syn}} < E_{m,f}^{\text{syn}}$ (Sari et al. 1999).

2.3. The Wind-to-ISM Transition

LGRBs are thought to be associated with the core collapse of massive stars, suggesting that the medium surrounding the progenitor is modified by the stellar wind. In the case of a Wolf-Rayet, for a mass-loss rate $\dot{M} \simeq 10^{-6} M_{\odot} \text{ yr}^{-1}$ with a wind velocity constant of $v_W \simeq 10^8 \text{ cm s}^{-1}$, the density of the stellar wind-type-like medium is given by $\rho(r) = A r^{-2}$, where $A = \frac{\dot{M}}{4\pi v_W} = A_{\star} (5 \times 10^{11}) \text{ g cm}^{-1}$ with A_{\star} a parameter of stellar wind density (Vink et al. 2000; Vink & de Koter 2005; Chevalier et al. 2004; Dai & Lu 1998; Dai & Wu 2003). The dynamics of the wind-to-ISM transition phase was originally introduced by Weaver et al. (1977) and Castor et al. (1975). Authors showed that this phase was made up of four-region structure which are (1) the unshocked stellar wind with density $\rho(r)$, (2) a quasi-isobaric zone consisting of the stellar wind mixed with a small fraction of interstellar gas, (3) a dense-thin shell formed by most of ISM and (4) the unshocked ambient ISM (see Figure 1 in Pe'er & Wijers 2006). Taking into consideration an adiabatic expansion, two strong shocks are formed, the outer and inner shocks. The outer termination (forward) shock radius can be estimated as

$$R_{FS,W} = \left(\frac{125}{308\pi} \right)^{\frac{1}{5}} \left(\frac{\dot{M} v_W^2 t_{\star}^3}{n} \right)^{\frac{1}{5}} \\ = 1.2 \times 10^{19} \text{ cm } \dot{M}_{-6}^{\frac{1}{5}} v_{W,8}^{\frac{2}{5}} n_0^{-\frac{1}{5}} t_{\star,5}^{-\frac{3}{5}}, \quad (1)$$

where t_{\star} is the lifetime of the Wolf-Rayet phase of the star and the homogeneous density has been written as $n = n_0 \text{ cm}^{-3}$.

The inner (reverse) shock radius for which the wind-to-ISM transition takes place (R_0 ; Pe'er & Wijers 2006) is calculated equating the pressures in zones (2) and (3)

$$P_{(2)} = P_{(3)} = \frac{7}{25} \left(\frac{125}{308\pi} \right)^{\frac{2}{5}} \left(\frac{\dot{M} v_W^2}{n t_{\star}^2} \right)^{\frac{2}{5}} \\ = 1.4 \times 10^{-11} \text{ dynes cm}^{-2} \dot{M}_{-6}^{\frac{2}{5}} v_{W,8}^{\frac{4}{5}} n_0^{-\frac{2}{5}} t_{\star,5}^{\frac{4}{5}} \quad (2)$$

with the strong conditions at the shock (e.g. see, Pe'er & Wijers 2006; Garcia-Segura & Franco 1996; Dai & Lu 2002). In this case the inner shock and the wind-to-ISM transition radius can be written as

$$R_0 \equiv R_{RS,W} = \left(\frac{3\dot{M} v_W}{16\pi P_{(2)}} \right) \\ = 5.1 \times 10^{18} \text{ cm } \dot{M}_{-6}^{\frac{3}{10}} v_{W,8}^{\frac{1}{10}} n_0^{-\frac{3}{10}} t_{\star,5}^{\frac{2}{5}}. \quad (3)$$

The density of stellar wind at $r = R_0$ is given by

$$\rho(R_0) = \frac{\dot{M}}{4\pi R_0^2 v_W} \\ = 1.8 \times 10^{-27} \text{ g cm}^{-3} R_0^{-2} \dot{M}_{-6} v_{W,8}^{-1}, \quad (4)$$

which corresponds to a number density of particles $1.1 \times 10^{-3} \text{ cm}^{-3}$.

3. GRB160625B: MULTIWAVELENGTH OBSERVATIONS, DATA REDUCTION AND DATA ANALYSIS

3.1. Multiwavelength observations and data reduction

At 22:40:16.28 UT, 2016 June 25, Fermi-GBM triggered and located GRB 160625B (Burns 2016). Later, at 22:43:24.82 UT, Fermi-LAT triggered on a luminous pulse of the ongoing burst. More than 300 photons were detected

above 100 MeV in the direction of this burst and the highest-energy photon detected was 15 GeV observed at 345 s after the GBM trigger (Dirirsa et al. 2016). XRT on board the Swift satellite followed up this burst for $\sim 1.1 \text{ ks}$ (Melandri et al. 2016). Surprisingly, at 22:51:16.03 GBM again triggered on this burst. Several optical observations were performed with the Pi of the Sky observatory, Mini-Mega TORTOLA, TSHAO, ABAO, Mondy, CrAO, Maidanak and SAO RAS (See; Zhang et al. 2016) and RATIR instrument (riZYJH bands; Troja et al. 2016). This burst also triggered Konus-Wind at 22:40:19.875 UT. Assuming the redshift $z=1.406$ (Xu et al. 2016), Konus-Wind measured the highest isotropic energy ever detected of $\sim 4 \times 10^{54} \text{ erg}$ (Svinkin et al. 2016). Fermi-LAT data in the energy range of 100 MeV - 300 GeV was reduced using the public database at the Fermi website¹. The lightcurve was obtained using the ScienceTools-v9r27p1 package and the P7TRANSIENT V6 response function. The Swift-XRT data used in this work are publicly available at the official Swift web site². The optical fluxes and their associated errors used in this work were calculated using the magnitudes reported by Zhang et al. (2016) with the standard conversion for AB magnitudes shown in Fukugita et al. (1996).

3.2. Multiwavelength data analysis

The Chi-square χ^2 minimization using the ROOT software package (Brun & Rademakers 1997) was done to fit the multiwavelength observations presented in the early and late afterglow. The values observed of decay slopes with their chi squares ($\chi^2 / \text{n.d.f.}$ ³) are reported in Table 1.

Due to connection between prompt emission and the early afterglow, we model the fast decay of the optical and LAT fluxes using the function

$$F(t) = A \left(\frac{t - t_0}{t_0} \right)^{-\alpha} e^{-\frac{\tau}{t - t_0}}, \quad (5)$$

where t_0 is the starting time, A is the amplitude, τ is the timescale of the flux rise and α is the temporal decay index (Vestrand et al. 2006). A blow-up of the optical and LAT light curves together with the modeling function before $\sim 700 \text{ sec}$ is shown in Figure 1. The best-fit values obtained of the optical (LAT) flux were $t_0 = 153.3 \pm 22.1 (142.4 \pm 9.8) \text{ s}$, $\tau = 101.2 \pm 9.3 (95 \pm 3.4) \text{ s}$ and $\alpha = 2.51 \pm 0.81 (2.46 \pm 0.75)$. The values of starting times suggest that both (LAT and optical) afterglow emission started simultaneously around $\sim 150 \text{ s}$. If a wrong t_0 is chosen to the precursor time, then some unreasonable results are obtained. However, if t_0 is chosen at the main burst, then the reasonable results as presented in the paper are obtained. This is understandable since the precursor is energetically insignificant. The blast wave dynamics is mostly defined by the main burst. On the other hand, the Fermi-LAT spectrum was plotted and modeled with a power law function (see Figure 2; left panel). The best-fit value found of the LAT spectral index is $\Gamma_{\text{LAT}} = \beta_{\text{LAT}} + 1 = 2.15 \pm 0.05$ and the observational LAT flux as function of time and energy is $F_{\nu} \propto t^{-2.46 \pm 0.75} E^{-1.15 \pm 0.05}$. Taking into consideration that during the early afterglow, this burst was only detected in the optical V-band, an extended dotted-dashed line over the only optical data was drawn. The value of the slope of 1.45 ± 0.05 for this line was chosen in accordance with the closure relation in our model. Deviations from those relations

¹ <http://fermi.gsfc.nasa.gov/ssc/data>

² <http://swift.gsfc.nasa.gov/cgi-bin/sdc/ql?>

³ Number of degrees of freedom

have been extensively analyzed in [Uhm & Zhang \(2014b\)](#). In this case, optical flux varies as $F_\nu \propto t^{-2.51 \pm 0.81} E^{-0.45 \pm 0.05}$. It is worth noting that the optical band is typically in the regime $E_{m,r}^{\text{syn}}(t_d) < E_{\text{opt}}^{\text{syn}} < E_{c,r}^{\text{syn}}(t_d)$ for ISM ([Zhang & Kobayashi 2005](#); [Kobayashi & Zhang 2003b](#)) and $E_{c,r}^{\text{syn}}(t_d) < E_{\text{opt}}^{\text{syn}} < E_{m,r}^{\text{syn}}(t_d)$ for stellar wind-type like medium ([Kobayashi & Zhang 2003a](#)). After the peak, the flux at an energy above $E_{c,r}^{\text{syn}}$ disappears at t_d because no electron is shocked anymore. For ISM, the cooling break energy is larger than the optical band ($E^{\text{syn}} < E_{c,r}^{\text{syn}}$) and the optical flux decays $\propto t^{-(73p+21)/96} \simeq t^{-2}$ ([Kobayashi 2000](#)). For stellar wind medium, the cooling break energy is smaller than the optical band ($E_{c,r}^{\text{syn}} < E^{\text{syn}}$) and the optical flux decays $\propto t^{-(\beta+2)}$ when the angular time delay effect produced by high latitude emission is considered ([Kobayashi & Zhang 2003a](#); [Kumar & Panaitescu 2000a](#)). Taking into consideration the value of spectral index $\beta_{\text{LAT}} = 1.15 \pm 0.05$, the LAT and optical fluxes are consistent with synchrotron and SSC emission in the fast-cooling regime for $p=2.4$ when the outflow is decelerated by the stellar wind medium. In order to find a correlation between GeV γ -ray and optical fluxes, the Pearson's correlation coefficients with the p-values are calculated. Considering a maximum allowed time difference between data of $\Delta t \lesssim 2, 5$ and 10 s, the Pearson's correlation coefficients are 0.93, 0.91 and 0.92 and the p values are 2.2×10^{-2} (i.e. the probability of being by chance is 1.2%), 6.6×10^{-4} and 1.1×10^{-8} , respectively. The values of these coefficients obtained during the period in which both GeV γ -ray and optical fluxes began to decline, reveal that GeV γ -ray and optical fluxes are strongly correlated and also that this correlation is not due to random chance. The observational (spectral an temporal) and theoretical values of the decay slopes (see Table 1) and the strong correlation between both fluxes are consistent with the theoretical values of synchrotron and SSC radiation from the reverse shock evolution in the stellar wind-type-like medium. This evolution corresponds to a thick-shell regime affected by the angular time delay effect (see, [Kobayashi & Zhang 2003a](#); [Kumar & Panaitescu 2000a](#)).

During the late afterglow from $\sim 8 \times 10^3$ to 6×10^6 s, X-rays and optical lightcurves were observed with a break at $t_j \sim 1.6 \times 10^6$ s. The slopes of the X-ray and optical fluxes before the break are $\alpha_{X,bb} = 1.327 \pm 0.521$ and $\alpha_{\text{opt},bb} = 0.921 \pm 0.163$, and after the breaks are $\alpha_{X,ab} = 2.348 \pm 0.860$ and $\alpha_{\text{opt},ab} = 2.036 \pm 0.521$, respectively. In addition, the spectrum energy distribution (SED) of the optical and X-ray data was modelled with a power law function (see Figure 2; right panel) and the best-fit value of $\Gamma_{X,\text{opt}} = \beta_{X,\text{opt}} + 1 = 1.71 \pm 0.12$ was obtained. Therefore, the flux varies as $F_\nu \propto t^{-1.327 \pm 0.521} E^{-0.71 \pm 0.12}$ and $F_\nu \propto t^{-0.921 \pm 0.163} E^{-0.71 \pm 0.12}$ for X-ray and optical wavelengths, respectively. These results indicate that the slopes observed for the X-ray and optical fluxes before the breaks are consistent with the forward-shock synchrotron emission in the slow-cooling regime ($E_{m,f}^{\text{syn}} < E^{\text{syn}} < E_{c,f}^{\text{syn}}$) for a power-law index of $p=2.4$ when outflow is decelerated by the ISM. After the breaks, post jet-break fluxes are proportional to $F_\nu \propto t^{-2.348 \pm 0.860} E^{-0.71 \pm 0.12}$ and $F_\nu \propto t^{-2.036 \pm 0.521} E^{-0.71 \pm 0.12}$ for X-ray and optical wavelengths, respectively, which are consistent with synchrotron radiation in the slow-cooling regime for $p=2.4$. The

observational and theoretical values are reported in Table 1. In general, using the reverse- and forward-shock light curves it can be seen that the early afterglow is consistent with the afterglow evolution in the wind medium and the late afterglow is consistent with the afterglow evolution in ISM. Table 1 shows that both values of slope decays (observational and theoretical) are in agreement.

Taking into account the starting time found of the LAT and optical afterglow $t_0 \approx 150$ s, the values of the bulk Lorentz factor Γ and the parameter A_* are constrained through the deceleration time in wind-type like medium $t_{d,\text{SW}}(\Gamma, A_*) \approx 150$ s. Taking into consideration that the early and late afterglows are consistent with radiation emitted when ejecta are decelerated in the stellar wind density and ISM, respectively, the wind-to-ISM transition must have taken place between ~ 700 s and $\sim 10^4$ s (see Fig. 1).

By using the values of the isotropic radiated energy $\sim 4 \times 10^{54}$ erg ([Svinkin et al. 2016](#)) with an efficiency $\eta \approx 0.2$ which corresponds to a kinetic energy of 2×10^{55} erg, the redshift $z=1.406$ ([Xu et al. 2016](#)), the spectral index of electron distribution $p = 2.4$ and the duration of the burst $T_{90} \simeq 188$ s, the fit in the early phase of the LAT and optical early data were done with synchrotron and SSC model in the stellar wind-type-like medium for a relativistic electron population radiating photons at 180 s with energies of 100 MeV and 2 eV, respectively. The late phase of the X-ray and optical data were modelled with synchrotron emission for the same relativistic electron population radiating photons at 5×10^4 s with energies of 5 keV and 2 eV, respectively. For $t \geq t_{j,\text{br}} \simeq 1.6 \times 10^6$ s, the post jet-break synchrotron light curves in the slow cooling regime for X-ray and optical fluxes are used.

4. RESULTS AND DISCUSSION

The multiwavelength data of the early afterglow (GeV and optical bands) and the late afterglow (X-rays and optical bands) are shown in Figure 1. In addition, we show the fit of the early afterglow using the afterglow evolution in the stellar wind-type-like medium and the late afterglow using the afterglow evolution in ISM. The values of the microphysical parameters and densities found with the fit of the multiwavelength observations and the wind-to-ISM transition are reported in Table 2. Using the values of the parameters in Table 2, we can infer the following:

1. Using the value found of the magnetic microphysical parameter after describing the early afterglow, the magnetization parameter becomes $\sigma \simeq 0.4$. This value means that ejecta is moderately magnetized and therefore, a successful reverse shock is expected. Otherwise, particle acceleration in the reverse shock is inefficient and the reverse shock would have been suppressed (for $\sigma \gg 1$). In addition, for $\sigma \gg 1$ the bright optical and LAT peaks would not have been detected ([Zhang & Kobayashi 2005](#); [Fan et al. 2004](#)). Several authors have pointed out that Poynting flux-dominated models with arbitrary magnetization could give account of the high-energy emission observed in the brightest LAT-detected bursts ([Uhm & Zhang 2014a](#); [Zhang & Yan 2011](#)). This value indicates that the ejecta must also have dissipated a significant amount of Poynting

- flux during the prompt emission phase, being the internal collision-induced magnetic reconnection and turbulence (ICMART) event the most favorable process to explain this pattern (Zhang & Yan 2011). This result agrees with the model proposed by Zhang et al. (2016) after analyzing the spectral properties exhibited in GRB 160625B. They suggested that the thermal and non-thermal emission coming from the events I and II could be explained through the transition from a fireball to Poynting flux-dominated jet.
2. The values of wind ($A_* = 0.2$) and ISM ($n=10 \text{ cm}^{-3}$) parameter densities found for the early and late afterglow, respectively, lie in the range of typical ones reported for highly energetic burst (Ackermann & et al. 2013; Perley et al. 2014; Vestrand et al. 2014; Fraija et al. 2012; Racusin et al. 2008). The values of circumburst medium $n=10 \text{ cm}^{-3}$ and the distance $z=1.406$ associated with this burst support the idea that the host could be a dwarf-irregular galaxy which has typical size of $L \sim 0.1 \text{ kpc}$ and column density of $N_H \simeq 3 \times 10^{21} \text{ cm}^{-2}$ (Bloom et al. 1998, 2001).
 3. Using the values of the parameters ($A_* = 0.2$) and ($n = 10 \text{ cm}^{-3}$), we derived the values of the wind-to-ISM transition for the deceleration time in the stellar wind and the transition radius which are $t_{d,W} = 7.8 \times 10^3 \text{ s}$ and $R_0 \simeq 2.6 \times 10^{18} \text{ cm}$, respectively. The value of initial bulk Lorentz factor derived in this afterglow model corresponds to $\Gamma=500$ similar to the LAT-detected bursts. By studying the spectral features of the LAT-detected bursts, Veres & Mészáros (2012) used a magnetically dominated ejecta model to describe the high-energy emission present in these energetic bursts. They showed that the inverse Compton scattering coming from the forward and reverse shocks give a significant contribution in the LAT emission, provided that the bulk Lorentz factor were in the range of 300- 600. In addition, other powerful bursts such as GRBs 110731A and 130427A were modelled using synchrotron and SSC emission from the external shock model for bulk Lorentz factors of 520 and 550, respectively. Considering that GRB 160625B is among the five most powerful bursts, it is expected that the value of the bulk Lorentz factor is in the range of the brightest LAT-detected bursts, as found in this work.

Table 3 shows the timescales, bulk Lorentz factors, synchrotron and SSC spectral breaks among others. These values were computed based on the values reported in Table 2 and the dynamics of a relativistic shell interacting with an stellar wind medium (Chevalier & Li 2000) and ISM (Sari et al. 1998) for the early and late afterglows, respectively. In accordance with the quantities reported in Table 3, the following results are found:

1. By comparing the synchrotron self-absorption energy ($E_{a,r}^{\text{syn}}$) with the characteristic ($E_{m,r}^{\text{syn}}$) and cooling ($E_{c,r}^{\text{syn}}$) energies obtained the early afterglow, it can be noted that synchrotron spectrum in the reverse shock lies in the weak self-absorption regime. Therefore, a thermal component generated by synchrotron radiation is not expected at $\sim 150 - 200 \text{ s}$.

2. The break observed in X-ray and optical light curves at $t_j \simeq 1.6 \times 10^6 \text{ s}$ is attributed to a jet break, leading to a jet opening angle of $\theta_j \simeq 8.3^\circ$ (Sari et al. 1999). The value of bulk Lorentz factor at the jet-break time corresponds to $\Gamma_{j,br} = 6.9$. The beaming corrected gamma-ray energy is then $3 \times 10^{52} \text{ erg}$ which makes it part of the hyper energetic GRBs (Cenko et al. 2011).
3. The maximum energy of synchrotron photons radiated in the stellar wind afterglow (the second event) is 7.69 GeV at 350 s. Then, the highest-energy photon of 15 GeV detected at 354 s after the GBM trigger is not consistent with the maximum synchrotron energy from an adiabatic forward shock propagating into the stellar wind of the star. Therefore, the most energetic photon could be explained by the inverse Compton scattering from the forward shock which has a characteristic break energy of 7.3 TeV.
4. During the early afterglow, a temporal correlation was found between the GeV γ -ray and optical bands. It suggests that the GeV γ -ray and optical fluxes were generated co-spatially by the same electron population. During the prompt and afterglow phases, correlations among distinct bands have been searched in order to explore the origin of the LAT-detected emission. For instance, an optical flash observed in the extremely brightest GRB 130427A correlated with the LAT-detected emission, indicating that both emissions originated in the early afterglow. A very similar pattern is found in GRB 160625B which displayed a bright optical flash in temporal correlation with the LAT emission. It suggests that the LAT emission could have been generated in the early afterglow.
5. The ratio of the magnetic fields in the forward- and reverse-shock regions found is $B_r/B_f \simeq 620$. The magnetic field in the reverse shock region is stronger than in the forward shock as found in the brightest LAT-detected burst (GRB 090510, GRB 110721A, GRB 110731A, GRB 130427A and others) the ejecta is magnetised. As follows we estimate the synchrotron flux contribution from the reverse and forward shocks. The forward-shock synchrotron quantities at $\sim 200 \text{ s}$ inferred from the later times are: $E_{m,f}^{\text{syn}} = 1.4 \text{ keV}$, $E_{c,f}^{\text{syn}} = 0.9 \text{ eV}$ and $F_{\text{max},f}^{\text{syn}} = 31.9 \text{ mJy}$, at $E^{\text{syn}} = 2 \text{ eV}$, flux is in the energy range of $E_{c,f}^{\text{syn}} < E^{\text{syn}} < E_{m,f}^{\text{syn}}$, and then it is given by $F_{\nu,f} = F_{\text{max},f}^{\text{syn}} \left(E^{\text{syn}}/E_{c,f}^{\text{syn}} \right)^{-1/2}$ (Sari et al. 1998). From the reverse-shock synchrotron quantities reported in Table 3, the reverse-shock synchrotron flux at $E^{\text{syn}} = 2 \text{ eV}$ lies in the energy range of $E_{m,r}^{\text{syn}} < E^{\text{syn}}$. Therefore, it can be written as $F_{\nu,r} = F_{\text{max},r}^{\text{syn}} \left(E_{m,r}^{\text{syn}}/E_{c,r}^{\text{syn}} \right)^{-1/2} \left(E^{\text{syn}}/E_{m,r}^{\text{syn}} \right)^{-p/2}$ (Sari et al. 1998). The synchrotron fluxes at forward and reverse shocks are $F_{\nu,f} = 21.4 \text{ mJy}$ and $F_{\nu,r} = 11.2 \times 10^2 \text{ mJy}$, respectively. These values in the fluxes indicate that synchrotron emission from the reverse shock is dominant over that radiation originated at the forward shock. The previous results together with the fact that the polarization percentage from the forward shocked circumburst medium is expected to be very low (see e.g.; Covino et al. 1999; Greiner et al. 2003) suggest that the optical flux is expected with some

degree of polarization.

6. GRB 160625B is one of the most energetic burst, suggesting a large amount of target photons for photo-hadronic interactions and then, making it a potential candidate for neutrino detection. However, no high-energy neutrinos in spatial and temporal coincidences were reported by the IceCube neutrino telescope around this burst. A similar powerful burst GRB 130427A with energy of $\sim 2 \times 10^{54}$ erg was detected by several satellites and ground-based telescopes (Maselli et al. 2014; Ackermann et al. 2014; Vestrand et al. 2014) and although searches for TeV - PeV neutrinos were performed, no excess were found above background. Gao et al. (2013b) stated that the neutrino non-detection could constrain the values of the bulk Lorentz factor, emitting radius and the energy fraction converted into cosmic rays ϵ_p . They found that almost independently of the bulk Lorentz factor, the energy fraction between electrons and cosmic rays lies in the range $\epsilon_p \lesssim \epsilon_e$. Although a robust analysis could be required, a simple proof can be done for GRB 160625B following a similar procedure. From our results obtained in early afterglow can be seen that the energy fraction given to accelerate electrons and amplified the magnetic field at the end of the prompt phase is $\epsilon_e = 0.5$ and $\epsilon_{B,r} = 0.4$, respectively. Taking into consideration the energy conservation condition $\epsilon_{B,r} + \epsilon_{e,r} + \epsilon_p \lesssim 1$, then the energy fraction converted into cosmic rays would be limited by $\epsilon_p \lesssim \frac{1}{2} \epsilon_e$. This result is very similar to that found by Gao et al. (2013b) for GRB 130427A and might explain the lack of high-energy neutrinos around GRB 160625B.
7. Kann et al. (2010) studied the optical photometry data in a total of 42 GRB afterglows. They found that 10% of the afterglows presented optical peaks followed by a fast decay which are usually associated with a reverse shock flash. Several authors have claimed that this kind of afterglow, as observed in GRB080319B (Racusin et al. 2008), GRB130427A (Ackermann et al. 2014; Vestrand et al. 2014), GRB050904 (Kann et al. 2007), GRB120711A (Martin-Carrillo et al. 2014), and GRB990123 (Akerlof et al. 1999), among others, are only present in the most luminous bursts. Given that GRB 160625B has been one of the most powerful bursts detected which exhibited an optical flash with a fast decay, this burst seems to confirm this statement and belong in the same category.

5. CONCLUSIONS

We have described the non-thermal multiwavelength observations of GRB 160625B collected with Fermi-LAT, Swift-XRT and several optical ground observatories. The

multiwavelength observations of the early afterglow are consistent with the afterglow evolution in a stellar wind medium. The optical spectral index is consistent with the synchrotron radiation while GeV γ -ray flux with SSC emission dominated by the high latitude emission. In this event, a strong correlation between GeV γ -ray and optical fluxes was found. On the other hand, the multiwavelength observations of the late afterglow are consistent with the afterglow evolution in ISM instead of the stellar wind profile. The X-ray and optical spectral indices in this event are consistent with synchrotron radiation from the adiabatic forward shock. The X-ray and optical flux decay indices after the break time of $\sim 1.6 \times 10^6$ s are softer than forward-shock synchrotron emission, being more consistent with the evolution of the jet after reaching a jet break. Using the observed jet break time of $\sim 1.6 \times 10^6$ s in X-ray and optical light curves, the opening angle of the jet and the bulk Lorentz factor at the jet break found are 8.3° and 6.9, respectively.

Optical and GeV γ -ray fluxes of the early afterglow were modeled with synchrotron and SSC emission from reverse shocks when the ultra-relativistic electrons are accelerated in the reverse shock evolving in the thick-shell regime. Optical and X-ray fluxes of late afterglow were fitted with synchrotron radiation from the adiabatic forward shocks. The inverse Compton scattering process from forward shock must be included in this afterglow model in order to explain the highest-energy photon of 15 GeV detected at 354 s after the GBM trigger. The values found of the wind density and ISM parameters are $A_* = 0.2$ and $n = 10 \text{ cm}^{-3}$. The value of ISM parameter found of this burst supports the idea that the host could be a dwarf-irregular galaxy. The values obtained in wind-to-ISM transition for the deceleration time in the stellar wind and transition radius are $t_{d,W} = 7.8 \times 10^3$ s and $R_0 \simeq 2.6 \times 10^{18}$ cm, respectively.

The value of the magnetization parameter $\sigma \simeq 0.4$ found after modelling the GeV γ -ray and optical fluxes in the early afterglow indicates that the Poynting flux-dominated jet models with arbitrary magnetization could give account about the spectral properties exhibited in GRB 160625B. Taking into consideration that the ejecta must be magnetized and the synchrotron emission from the reverse shock is stronger than the radiation originated in the forward shock, then optical polarization is expected from the reverse-shock region.

The value found of the initial bulk Lorentz factor $\Gamma \simeq 500$, and the bright optical flash with a fast decay reported in this burst indicates that GRB 160625B shares similarities with the most luminous LAT and pre-LAT era events, consistent with GRB160625B being one of the most extreme GRBs regarding energy output.

We thank the anonymous referee for valuable suggestions that helped improve our manuscript. We thank Simone Dichiaro, Fabio De Colle and Alexander A. Kann for useful discussions. NF acknowledges financial support from UNAM-DGAPA-PAPIIT through grant IA102917 and WHL through grant 100317. PV thanks Fermi grant NNM11AA01A and partial support from OTKA NN 111016 grant.

REFERENCES

- Ackermann, M., & et al. 2013, ApJ, 763, 71
 Ackermann, M., Ajello, M., Asano, K., et al. 2013, ApJS, 209, 11
 —. 2014, Science, 343, 42
 Akerlof, C., Balsano, R., Barthelmy, S., et al. 1999, Nature, 398, 400
 Bloom, J. S., Djorgovski, S. G., & Kulkarni, S. R. 2001, ApJ, 554, 678

- Bloom, J. S., Djorgovski, S. G., Kulkarni, S. R., & Frail, D. A. 1998, *ApJ*, 507, L25
- Bromberg, O., Nakar, E., Piran, T., & Sari, R. 2011, *ApJ*, 740, 100
- Brun, R., & Rademakers, F. 1997, *Nuclear Instruments and Methods in Physics Research A*, 389, 81
- Burns, E. 2016, *GRB Coordinates Network*, 19581
- Castor, J., McCray, R., & Weaver, R. 1975, *ApJ*, 200, L107
- Cenko, S. B., Frail, D. A., Harrison, F. A., et al. 2011, *ApJ*, 732, 29
- Chevalier, R. A., & Li, Z.-Y. 1999, *ApJ*, 520, L29
- . 2000, *ApJ*, 536, 195
- Chevalier, R. A., Li, Z.-Y., & Fransson, C. 2004, *ApJ*, 606, 369
- Coburn, W., & Boggs, S. E. 2003, *Nature*, 423, 415
- Covino, S., Lazzati, D., Ghisellini, G., et al. 1999, *A&A*, 348, L1
- Dai, Z. G., & Lu, T. 1998, *MNRAS*, 298, 87
- . 2002, *ApJ*, 565, L87
- Dai, Z. G., & Wu, X. F. 2003, *ApJ*, 591, L21
- Dirirsa, F., Vianello, G., Racusin, J., & Axelsson, M. 2016, *GRB Coordinates Network*, 19586
- Fan, Y. Z., Wei, D. M., & Wang, C. F. 2004, *A&A*, 424, 477
- Frajia, N. 2015, *ApJ*, 804, 105
- Frajia, N., González, M. M., & Lee, W. H. 2012, *ApJ*, 751, 33
- Frajia, N., Lee, W., & Veres, P. 2016a, *ApJ*, 818, 190
- Frajia, N., Lee, W. H., Veres, P., & Barniol Duran, R. 2016b, *ApJ*, 831, 22
- Fukugita, M., Ichikawa, T., Gunn, J. E., et al. 1996, *AJ*, 111, 1748
- Gao, H., Lei, W.-H., Zou, Y.-C., Wu, X.-F., & Zhang, B. 2013a, *New Astronomy Reviews*, 57, 141
- Gao, H., Wang, X.-G., Mészáros, P., & Zhang, B. 2015, *ApJ*, 810, 160
- Gao, S., Kashiyama, K., & Mészáros, P. 2013b, *ApJ*, 772, L4
- Garcia-Segura, G., & Franco, J. 1996, *ApJ*, 469, 171
- Gorbovskoy, E. S., Lipunov, V. M., Buckley, D. A. H., et al. 2016, *MNRAS*, 455, 3312
- Greiner, J., Klose, S., Reinsch, K., et al. 2003, *Nature*, 426, 157
- Hjorth, J., & Bloom, J. S. 2012, *The Gamma-Ray Burst - Supernova Connection*, 169–190
- Hjorth, J., Sollerman, J., Møller, P., et al. 2003, *Nature*, 423, 847
- Huang, X.-L., Xin, L.-P., Yi, S.-X., et al. 2016, *ApJ*, 833, 100
- Kann, D. A., Masetti, N., & Klose, S. 2007, *AJ*, 133, 1187
- Kann, D. A., Klose, S., Zhang, B., et al. 2010, *ApJ*, 720, 1513
- Kobayashi, S. 2000, *ApJ*, 545, 807
- Kobayashi, S., & Zhang, B. 2003a, *ApJ*, 597, 455
- . 2003b, *ApJ*, 582, L75
- Kobayashi, S., Zhang, B., Mészáros, P., & Burrows, D. 2007, *ApJ*, 655, 391
- Kopač, D., Mundell, C. G., Japelj, J., et al. 2015, *ApJ*, 813, 1
- Kumar, P., & Panaitescu, A. 2000a, *ApJ*, 541, L51
- . 2000b, *ApJ*, 541, L9
- Kumar, P., & Zhang, B. 2015, *Phys. Rep.*, 561, 1
- Lü, H.-J., Lü, J., Zhong, S.-Q., et al. 2017, *ArXiv e-prints*, arXiv:1702.01382
- Martin-Carrillo, A., Hanlon, L., Topinka, M., et al. 2014, *A&A*, 567, A84
- Maselli, A., Melandri, A., Nava, L., et al. 2014, *Science*, 343, 48
- Melandri, A., D’Avanzo, P., D’Elia, V., et al. 2016, *GRB Coordinates Network*, 19585
- Mizuta, A., & Ioka, K. 2013, *ApJ*, 777, 162
- Mundell, C. G., Steele, I. A., Smith, R. J., et al. 2007, *Science*, 315, 1822
- Mundell, C. G., Kopač, D., Arnold, D. M., et al. 2013, *Nature*, 504, 119
- Panaitescu, A., & Kumar, P. 2000, *ApJ*, 543, 66
- . 2002, *ApJ*, 571, 779
- Pe’er, A., & Wijers, R. A. M. J. 2006, *ApJ*, 643, 1036
- Perley, D. A., Cenko, S. B., Corsi, A., et al. 2014, *ApJ*, 781, 37
- Pruzhinskaya, M. V., Krushinsky, V. V., Lipunova, G. V., et al. 2014, *New A*, 29, 65
- Racusin, J. L., Karpov, S. V., Sokolowski, M., et al. 2008, *Nature*, 455, 183
- Ramirez-Ruiz, E., Celotti, A., & Rees, M. J. 2002, *MNRAS*, 337, 1349
- Rhoads, J. E. 1999, *ApJ*, 525, 737
- Sari, R., Piran, T., & Halpern, J. P. 1999, *ApJ*, 519, L17
- Sari, R., Piran, T., & Narayan, R. 1998, *ApJ*, 497, L17
- Steele, I. A., Mundell, C. G., Smith, R. J., Kobayashi, S., & Guidorzi, C. 2009, *Nature*, 462, 767
- Svinkin, D., Golenetskii, S., Aptekar, R., et al. 2016, *GRB Coordinates Network*, 19604
- Taylor, G. B., Frail, D. A., Berger, E., & Kulkarni, S. R. 2004, *ApJ*, 609, L1
- Troja, E., Butler, N., Watson, A. M., et al. 2016, *GRB Coordinates Network*, 19588
- Troja, E., Lipunov, V. M., Mundell, C. G., et al. 2017, *Nature*, 547, 425
- Uhm, Z. L., & Zhang, B. 2014a, *Nature Physics*, 10, 351
- . 2014b, *ApJ*, 780, 82
- Usov, V. V. 1992, *Nature*, 357, 472
- van Eerten, H., Zhang, W., & MacFadyen, A. 2010, *ApJ*, 722, 235
- Veres, P., & Mészáros, P. 2012, *ApJ*, 755, 12
- Vestrand, W. T., Wren, J. A., Wozniak, P. R., et al. 2006, *Nature*, 442, 172
- Vestrand, W. T., Wren, J. A., Panaitescu, A., et al. 2014, *Science*, 343, 38
- Vink, J. S., & de Koter, A. 2005, *A&A*, 442, 587
- Vink, J. S., de Koter, A., & Lamers, H. J. G. L. M. 2000, *A&A*, 362, 295
- Wang, X. Y., Dai, Z. G., & Lu, T. 2001a, *ApJ*, 546, L33
- . 2001b, *ApJ*, 556, 1010
- Weaver, R., McCray, R., Castor, J., Shapiro, P., & Moore, R. 1977, *ApJ*, 218, 377
- Wheeler, J. C., Yi, I., Höflich, P., & Wang, L. 2000, *ApJ*, 537, 810
- Woodsley, S. E., & Bloom, J. S. 2006, *ARA&A*, 44, 507
- Xu, D., Malesani, D., Fynbo, J. P. U., et al. 2016, *GRB Coordinates Network*, 19600
- Zhang, B., & Kobayashi, S. 2005, *ApJ*, 628, 315
- Zhang, B., Kobayashi, S., & Mészáros, P. 2003, *ApJ*, 595, 950
- Zhang, B., & Yan, H. 2011, *ApJ*, 726, 90
- Zhang, B.-B., Zhang, B., Castro-Tirado, A. J., et al. 2016, *ArXiv e-prints*, arXiv:1612.03089

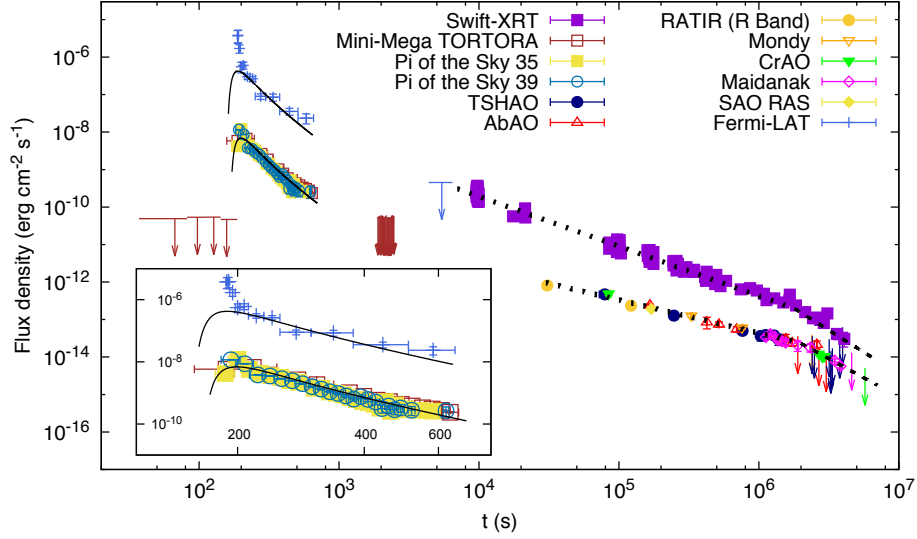


FIG. 1.— Light curves and fits of the multiwavelength (LAT, XRT and UVOT) observation of GRB 160625B with our external shock model. We use the LC of RS in the thick-shell regime to describe the bright LAT-peak flux (continuous line), the LC of FS to explain the temporally extended LAT, X-ray and optical emissions before the break time at $t_{br} \sim 1.5 \times 10^3$ s (dotted lines) and the LC after the jet break time (dashed lines). Fermi-LAT data were reduced using the public database at the Fermi website, the Swift-XRT data were obtained using the publicly available database at the official Swift web site, optical data (Mini-Mega TORTORA, Pi of the Sky 35 and 39, TSHAO, AbAO, Mondy, CrAO, Maidanak and SAO RAS) were collected from Zhang et al. (2016) and RATIR R-band data were obtained from Troja et al. (2016). The initial time of this plot is the onset of the small precursor event detected by the Fermi-GBM

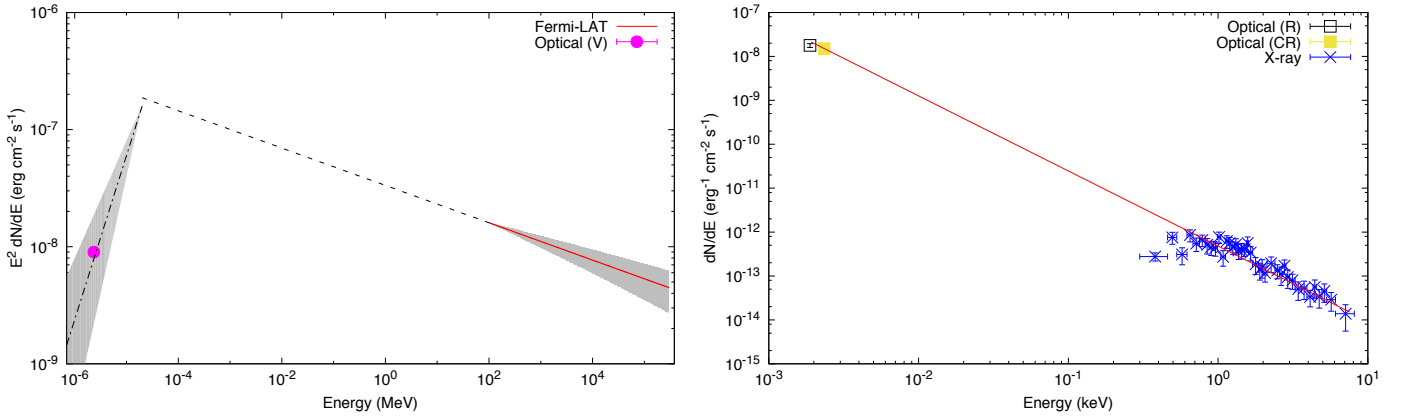


FIG. 2.— Left panel: SED of the Fermi-LAT and optical observations of the early afterglow. Right panel: SED of the X-ray and optical observations of the late afterglow. Optical R-, CR- and V-band data were average over each band.

Table 1. Fitted values of the multiwavelength data. Values in round parenthesis are the chi-square minimization ($\chi^2 / \text{n.d.f.}$)

		Early afterglow		Late afterglow	
		Observation	Theory	Observation	Theory
GeV flux					
Decay slope	α_{LAT}	2.46 ± 0.75 (44.77/10)	3.20	–	
Spectral slope	β_{LAT}	1.15 ± 0.05 (35.6/31)	1.20	–	
X-ray flux					
Decay slope (before break)	$\alpha_{X,bb}$	–	1.327 ± 0.521 (156.5/112)		1.05
Decay slope (after break)	$\alpha_{X,ab}$	–	2.348 ± 0.860 (4.869/6)		2.40
Break time (s)	$t_{X,br}$	–		1.64×10^6	
Spectral slope	β_X	–	0.71 ± 0.12 (156.5/112)		0.70
Optical flux					
Early decay slope	$\alpha_{opt,e}$	2.51 ± 0.81 (1588/50)	2.50	–	
Decay slope (before break)	$\alpha_{opt,bb}$	–		0.921 ± 0.163 (36.9/28)	1.05
Decay slope (after break)	$\alpha_{opt,ab}$	–		2.036 ± 0.521 (8.91/6)	2.40
Break time (s)	$t_{o,br}$	–		1.71×10^6	
Late spectral slope	β_{opt}	–		0.71 ± 0.12 (156.5/112)	0.70

Table 2. Parameters found of the early and late afterglow.

Early afterglow		Late afterglow	
$\epsilon_{B,r}$	0.40 ± 0.04	$\epsilon_{B,f}$	$(1.1 \pm 0.1) \times 10^{-6}$
$\epsilon_{e,r}$	0.45 ± 0.05	$\epsilon_{e,f}$	0.45 ± 0.05
A_\star	0.20 ± 0.02	n (cm $^{-3}$)	10.0 ± 0.1

Table 3. Quantities derived with our leptonic model for the early and late afterglow. Quantities for the early afterglow are calculated at 150 s and for the late afterglow at 5×10^4 s. At the jet-break time (1.6×10^6 s), the jet opening angle and the bulk Lorentz factor are 8.3° and 6.9, respectively.)

Early afterglow		Late afterglow	
Γ_c	397.5 ± 26.9		
B_r (G)	123.9 ± 58.3	B_f (G)	$(2.1 \pm 0.3) \times 10^{-1}$
Γ	500	Γ	25.2 ± 7.8
Synchrotron			
$E_{a,r}^{syn}$ (eV)	$(1.3 \pm 0.4) \times 10^{-9}$	$E_{a,f}^{syn}$ (eV)	$(7.7 \pm 3.1) \times 10^{-5}$
$E_{m,r}^{syn}$ (eV)	2.1 ± 0.5	$E_{m,f}^{syn}$ (eV)	0.4 ± 0.1
$E_{c,r}^{syn}$ (eV)	$(2.5 \pm 0.7) \times 10^{-5}$	$E_{c,f}^{syn}$ (keV)	125.8 ± 32.6
SSC			
$E_{m,r}^{ssc}$ (MeV)	90.5 ± 26.9		
$E_{c,r}^{ssc}$ (keV)	$(1.0 \pm 0.1) \times 10^{-3}$		